Supporting Information

Pressure-Induced Spin Transition and Emergence of ϕ Bond in Actinide Sandwich Complexes $An^{III}(COT)_2^-/An^{IV}(COT)_2$ (An = U, Np, Pu)

Xiaocheng Xu, Chengliang Xiao*

College of Chemical and Biological Engineering, Zhejiang University, Hangzhou, 310058, China

*E-mail: xiaoc@zju.edu.cn (Chengliang Xiao)

Method and Computational Details

1. The choice of PBE functional and *k*-point tests.

While hybrid functionals can in principle offer an improved description of localized f-electron states, their application to periodic systems under extreme pressures combined with multiple competing spin states is, in practice, computationally prohibitive. In the present work, the calculations involve large periodic cells, pressures up to several hundred gigapascals, and systematic exploration of multiple spin configurations at each pressure point. Under these conditions, the use of hybrid functionals is not feasible within a reasonable computational cost. For these reasons, we employed the PBE functional,[1] which has been widely and successfully used in previous high-pressure studies of actinide systems and is known to provide a consistent description of pressure-induced structural and electronic trends.[2, 3] Importantly, our study focuses on relative pressure-dependent trends, such as changes in bonding characteristics, orbital interactions, and spin-state, rather than on absolute energetics. To ensure internal consistency and comparability across all pressures, elements, and spin states, we therefore adopted the PBE functional throughout the entire study. For the K-points test, the 1×1×1, 2×2×2, 3×2×2 and other meshes were examined and the tested total energies of $U^{IV}(COT)_2$ at different K-points are shown in Figure S1. The results show that the accuracy is already well converged at the 2×2×2 level. Considering both accuracy and computational cost, the 2×2×2 k-point mesh was adopted in this work.

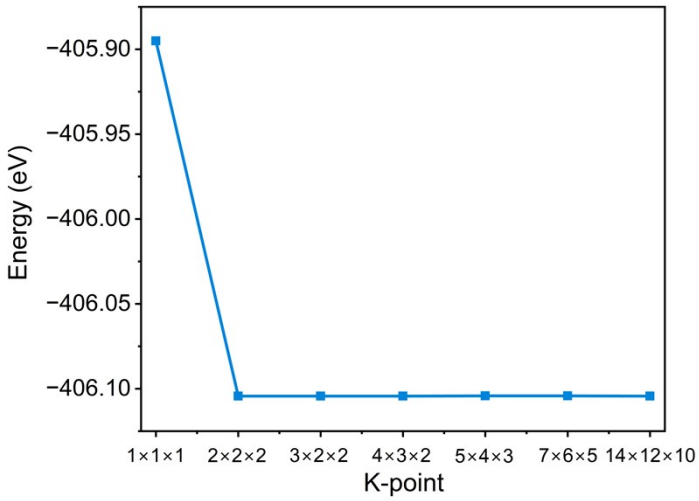

Figure S1. The test total energy of $U^{IV}(COT)_2$ at different K-points.

2. The assessment of functionals.

To assess the reliability of the PBE functional in predicting spin transition pressures. We have performed additional benchmark calculations using the OLYP functional,[4] which is known to perform well for spin-crossover properties among GGAs, as well as the hybrid PBE0 functional.[5] Besides, we have performed additional benchmark calculations using the double hybrid functional B2PLYP-D3BJ[6,] as well as two range-separated functionals, CAM-B3LYP[7] and LCY-BLYP[8]. The corresponding results are summarized in Tables S1-6. From these data, we find that although the absolute total bonding energies, the energy differences between the singlet and triplet states, orbital interaction term (E_{orb}) and orbital components show some quantitative variations depending on the functional employed, the overall trends are fully consistent across all three functionals. For instance, for $U^{IV}(COT)_2$, all functionals predict a spin transition occurring in the 80-120 GPa pressure range, while for $U^{III}(COT)_2^-$ the spin transition is also consistently found within the 40-80 GPa range. These results demonstrate that, despite functional-dependent shifts in absolute energetics, the predicted pressure window for spin transition is robust and does not depend sensitively on the choice of exchange-correlation functional. We therefore conclude that the PBE functional provides a reliable description of the pressure-induced spin transition behavior in the present systems.

Table S1. The total energy of different states of $U^{IV}(COT)_2$ at different pressures (kcal·mol^{-1}).

$U^{IV}(COT)_2$	PBE			OLYP			PBE0		
Pressure/GPa	singlet	triplet	Δ*E*	singlet	triplet	Δ*E*	singlet	triplet	Δ*E*
0	-4852.09	-4859.40	7.31	-4656.45	-4666.58	10.13	-5890.27	-5905.76	15.49
40	-4786.39	-4789.94	3.55	-4592.56	-4597.27	4.71	-5842.52	-5847.89	5.37
80	-4687.66	-4688.18	0.52	-4495.36	-4495.78	0.42	-5745.94	-5746.18	0.24
120	-4592.32	-4590.18	-2.14	-4400.14	-4398.52	-1.62	-5646.11	-5644.81	-1.30
160	-4507.75	-4502.95	-4.80	-4317.49	-4313.05	-4.44	-5558.77	-5554.29	-4.48
200	-4357.54	-4348.77	-8.77	-4166.59	-4158.46	-8.13	-5398.09	-5391.18	-6.91

Table S2. The total energy of different states of $U^{III}(COT)_2^-$ at different pressures (kcal·mol^{-1}).

$U^{III}(COT)_2^-$	PBE			OLYP			PBE0		
Pressure/GPa	singlet	triplet	Δ*E*	singlet	triplet	Δ*E*	singlet	triplet	Δ*E*
0	-4860.56	-4872.17	11.61	-4664.44	-4678.40	13.96	-5919.79	-5939.14	19.25
40	-4813.84	-4819.89	6.05	-4616.83	-4624.56	7.73	-5856.87	-5864.56	7.69
80	-4720.89	-4717.87	-3.02	-4522.33	-4520.89	-1.44	-5774.72	-5769.98	-4.74
120	-4621.37	-4615.01	-6.36	-4424.59	-4420.02	-4.57	-5672.36	-5663.30	-9.06
160	-4541.68	-4530.61	-11.07	-4345.83	-4336.40	-9.43	-5589.78	-5578.45	-11.33
200	-4460.40	-4445.61	-14.79	-4266.75	-4253.26	-13.49	-5506.00	-5486.67	-19.33

Table S3. The total energy of different states of $U^{IV}(COT)_2$ at different pressures (kcal·mol^{-1}).

$U^{IV}(COT)_2$	B2PLYP-D3BJ			CAM-B3LYP			LCY-BLYP		
Pressure/GPa	singlet	triplet	Δ*E*	singlet	triplet	Δ*E*	singlet	triplet	Δ*E*
0	-7145.16	-7157.44	12.28	-6755.72	-6773.34	17.62	-7973.53	-7989.33	15.80
40	-7084.76	-7093.89	9.13	-6699.72	-6707.76	8.04	-7934.89	-7941.52	6.63
80	-6976.91	-6980.68	3.77	-6601.98	-6603.64	1.66	-7840.63	-7841.53	0.90
120	-6869.74	-6865.92	-3.82	-6493.52	-6491.99	-1.53	-7742.26	-7739.80	-2.46
160	-6787.98	-6779.60	-8.38	-6410.64	-6405.85	-4.79	-7654.62	-7650.34	-4.28
200	-6625.34	-6614.38	-10.96	-6236.40	-6229.87	-6.53	-7477.24	-7471.54	-5.70

Table S4. The total energy of different states of $U^{III}(COT)_2^-$ at different pressures (kcal·mol^{-1}).

$U^{III}(COT)_2^-$	B2PLYP-D3BJ			CAM-B3LYP			LCY-BLYP		
Pressure/GPa	singlet	triplet	Δ*E*	singlet	triplet	Δ*E*	singlet	triplet	Δ*E*
0	-7157.50	-7182.38	24.88	-6754.69	-6777.32	22.63	-7995.97	-8023.59	27.62
40	-7103.98	-7113.59	9.61	-6731.46	-6738.85	7.39	-7944.41	-7952.64	8.23
80	-7012.33	-7009.78	-2.55	-6623.69	-6620.12	-3.57	-7856.32	-7851.21	-5.11
120	-6894.91	-6891.27	-3.64	-6521.11	-6516.96	-4.15	-7759.68	-7754.39	-5.29
160	-6823.56	-6809.85	-13.71	-6435.72	-6426.53	-9.19	-7676.16	-7668.29	-7.87
200	-6734.77	-6717.97	-16.80	-6799.69	-6783.82	-15.87	-7594.04	-7579.35	-14.69

Table S5. The orbital interaction term (E_{orb}) from the EDA-NOCV analysis of $U^{IV}(COT)_2$ with different functionals at different pressures (kcal·mol^{-1}).

Pressure/GPa	PBE	PBE0	B2PLYP-D3BJ	CAM-B3LYP	LCY-BLYP
0	-917.72	-958.08	-1003.82	-1019.62	-1028.23
40	-1151.94	-1185.60	-1223.45	-1191.89	-1252.71
80	-1360.68	-1354.20	-1392.28	-1348.30	-1405.87
120	-1495.54	-1518.89	-1501.09	-1447.58	-1503.75
160	-1607.74	-1569.72	-1605.49	-1544.56	-1601.39
200	-1765.03	-1725.16	-1747.39	-1724.68	-1743.68

Table S6. The orbital components analysis of $U^{IV}(COT)_2$ with different functionals at 200 GPa.

Orbital	Contribution	PBE	PBE0	B2PLYP-D3BJ	CAM-B3LYP	LCY-BLYP
HOMO	5f%	36.6	39.1	39.7	42.0	41.6
	2p%	63.4	60.9	60.3	58.0	58.4
HOMO-1	5f%	30.7	30.2	29.7	33.4	31.9
	2p%	69.3	69.8	70.3	66.6	68.1

3. The assessment of scalar ZORA/X2C and frozen core approximation.

The 4f orbitals were included in the frozen core primarily because they are significantly more contracted than the 5f orbitals and, in most cases, do not participate directly in chemical bonding. In addition, the 4f shell is fully occupied ($4f^{14}$), and its contribution to bonding interactions is generally negligible compared to that of the more spatially extended 5f orbitals. Nevertheless, considering the possibility that extreme compression may enhance the involvement of inner-shell orbitals under very high pressure, we explicitly assessed the validity of the frozen-core approximation by comparing calculations employing a frozen $4f^{14}$ core with corresponding all-electron calculations. These tests show that the 4f orbitals remain largely inert and do not contribute appreciably to the bonding interactions or to the pressure-induced electronic trends discussed in this work.

Furthermore, to examine the interplay between relativistic effects and the frozen-core approximation, we performed additional calculations using different relativistic treatments, including scalar ZORA and X2C (Table S7).[9-11] The resulting electronic structures and bonding

characteristics are found to be consistent across these approaches, indicating that scalar ZORA are sufficient to capture the essential physics of the present systems.

Table S7. The 5f contribution to selected bonding orbitals of $An^{III}(COT)_2^-$/$An^{IV}(COT)_2$ with different computational levels at 200 GPa.

Compounds	Orbital	scalar ZORA +core($1s^2$-$4f^{14}$)	scalar X2C +core($1s^2$-$4f^{14}$)	scalar ZORA +all electron	scalar X2C +all electron
$U^{IV}(COT)_2$	HOMO	36.6%	31.7%	32.7%	28.0%
$Np^{IV}(COT)_2$	SOMO	52.8%	48.7%	58.0%	55.1%
$Pu^{IV}(COT)_2$	SOMO	48.1%	46.9%	49.2%	48.6%
$U^{III}(COT)_2^-$	SOMO	54.1%	52.2%	58.6%	55.4%
$Np^{III}(COT)_2^-$	SOMO-1	45.4%	46.0%	47.8%	47.6%
$Pu^{III}(COT)_2^-$	SOMO	78.4%	84.5%	81.9%	83.4%

4. Computational Methods of CASSCF.

All multiconfigurational wavefunction calculations were carried out with the ORCA 5.0.4 quantum chemistry package.[12] Scalar-relativistic effects for the actinide centers (U, Np, Pu) were treated using the Stuttgart basis sets and the corresponding energy-consistent effective core potentials (ECP78MWB for U, ECP80MWB for Np and ECP82MWB for Pu).[13] The corresponding valence basis sets were employed for the actinide atoms. The carbon atoms were also described using the Stuttgart ECP2MWB effective core potential,[14] together with the corresponding valence basis set, while hydrogen atoms were treated at the DKH-def2-SVP level.[15]

5. The benchmarking against CASSCF.

The benchmarking against higher-level wavefunction-based methods is crucial for systems where unconventional bonding and spin-state behavior are predicted. We performed additional CASSCF/CASPT2[16-20] calculations of $An^{III}(COT)_2^-$/$An^{IV}(COT)_2$ at 200 GPa (Table S8-9). The results show that, consistent with DFT predictions, the low-spin state is energetically favored over the high-spin state at 200 GPa pressure. This confirms the pressure-induced spin transition reported in our work. Moreover, we provide the representative CASSCF natural orbitals of $An^{III}(COT)_2^-$/$An^{IV}(COT)_2$ at 200 GPa (Figure S2), which exhibit the same qualitative features as those obtained

from DFT. In particular, the characteristic ϕ type bonding interaction is clearly preserved at the CASSCF level, further validating the robustness of our bonding interpretation.

Table S8. The energy of low/high-spin state of $An^{III}(COT)_2^-$/$An^{IV}(COT)_2$ at CASSCF level at 200 GPa (a.u.).

Compounds	Basis set/LC-ECP	active space	low spin	high spin
$U^{IV}(COT)_2$	ECP78MWB	CAS(10,10)	-146.491	-146.464
$U^{III}(COT)_2^-$	ECP78MWB	CAS(11,10)	-146.579	-146.558
$Np^{IV}(COT)_2$	ECP80MWB	CAS(9,10)	-140.232	-140.172
$Np^{III}(COT)_2^-$	ECP80MWB	CAS(10,10)	-140.253	-140.225
$Pu^{IV}(COT)_2$	ECP82MWB	CAS(8,10)	-134.220	-134.163
$Pu^{III}(COT)_2^-$	ECP82MWB	CAS(9,10)	-134.326	-134.211

Table S9. The energy of low/high-spin state of $An^{III}(COT)_2^-$/$An^{IV}(COT)_2$ at CASPT2 level at 200 GPa (a.u.).

Compounds	Basis set/LC-ECP	active space	low spin	high spin
$U^{IV}(COT)_2$	ECP78MWB	CAS(10,10)	-148.744	-148.732
$U^{III}(COT)_2^-$	ECP78MWB	CAS(11,10)	-148.755	-148.742
$Np^{IV}(COT)_2$	ECP80MWB	CAS(9,10)	-142.537	-142.529
$Np^{III}(COT)_2^-$	ECP80MWB	CAS(10,10)	-142.556	-142.543
$Pu^{IV}(COT)_2$	ECP82MWB	CAS(8,10)	-136.447	-136.428
$Pu^{III}(COT)_2^-$	ECP82MWB	CAS(9,10)	-136.452	-136.436

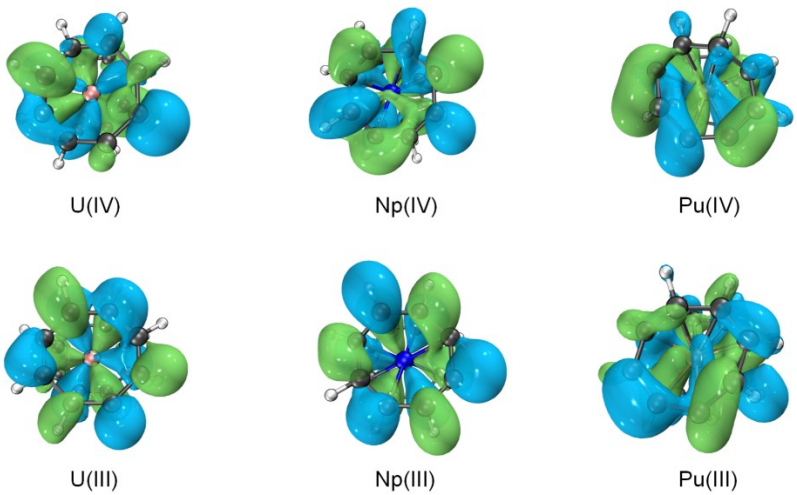

Figure S2. The representative CASSCF natural orbitals of $An^{III}(COT)_2^-$/$An^{IV}(COT)_2$ at 200 GPa (isosurface = 0.02 a.u.)

6. The analysis of vibrational frequency.

The phonon dispersion calculations were performed for the molecular solid $U^{IV}(COT)_2$ over the pressure range of 0-200 GPa using density-functional perturbation theory (DFPT)[21,22] within a 1×1×1 primitive cell (Figure S3-5). Owing to the molecular-crystal nature of the system, the phonon spectra at different pressures exhibit nearly parallel dispersion features, indicating that the overall lattice dynamical behavior is preserved upon compression. Small imaginary frequencies are observed only in a limited low-frequency region and are of very small magnitude. Such minor imaginary modes are commonly encountered in high-pressure phonon calculations of molecular solids, particularly for systems containing heavy actinide elements. While employing larger supercells could further suppress these artifacts, the associated computational cost for the present U-containing systems would be prohibitively high. Importantly, these small imaginary frequencies do not affect the relative energetic trends or the conclusions drawn in this work.

In addition, to further assess the intrinsic stability of the molecular units, vibrational frequency calculations were carried out for isolated molecular models of the U, Np, and Pu analogues. At 0 GPa, all molecular structures correspond to true minima with no imaginary frequencies. At elevated pressures, small imaginary frequencies are found, which is expected because these geometries are extracted directly from the compressed solid-state structures and cannot be fully geometry-optimized; otherwise, the structures would relax back toward their ambient-pressure

configurations. Similar treatments and observations have been widely reported in high-pressure molecular studies.[2, 3] Regarding the thermodynamic aspect, the resulting Δ*G*-pressure curves show a monotonic increase in Δ*G* with increasing pressure (Figure S6), fully consistent with the trends obtained from the energy decomposition analysis (EDA) based on total energies. This behavior is physically reasonable, as $U^{IV}(COT)_2$ is most stable under ambient conditions, and increasing pressure introduces additional structural strain and electronic destabilization.

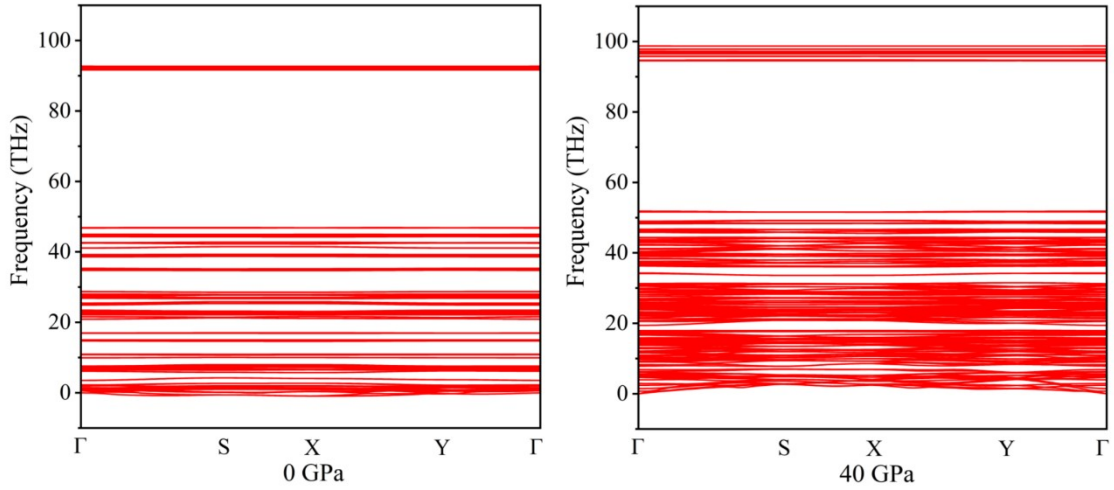

Figure S3. The phonon dispersion curves of $U^{IV}(COT)_2$ calculated at 0 and 40 GPa.

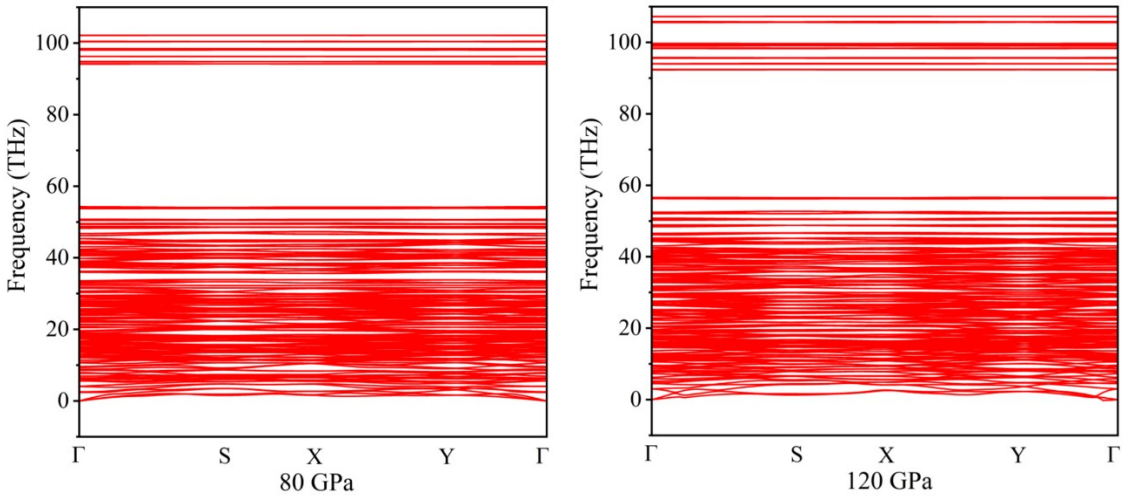

Figure S4. The phonon dispersion curves of $U^{IV}(COT)_2$ calculated at 80 and 120 GPa.

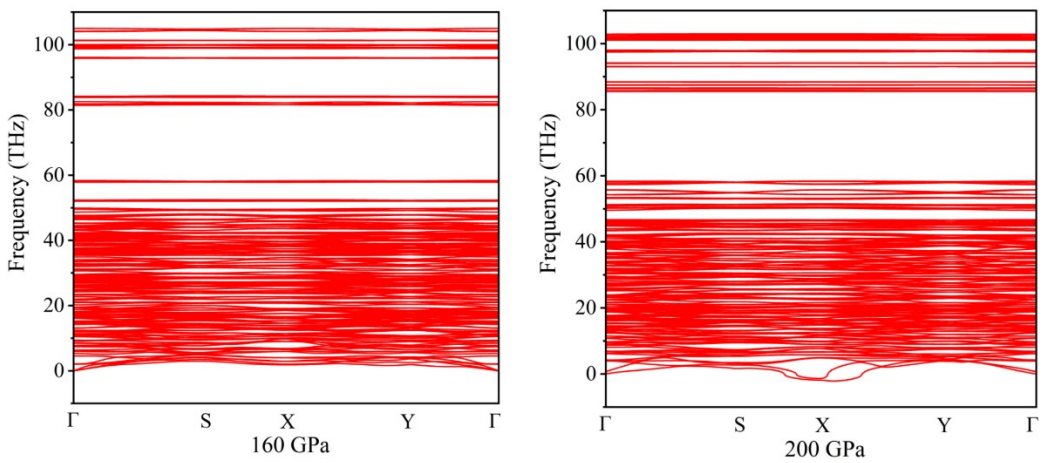

Figure S5. The phonon dispersion curves of $U^{IV}(COT)_2$ calculated at 160 and 200 GPa.

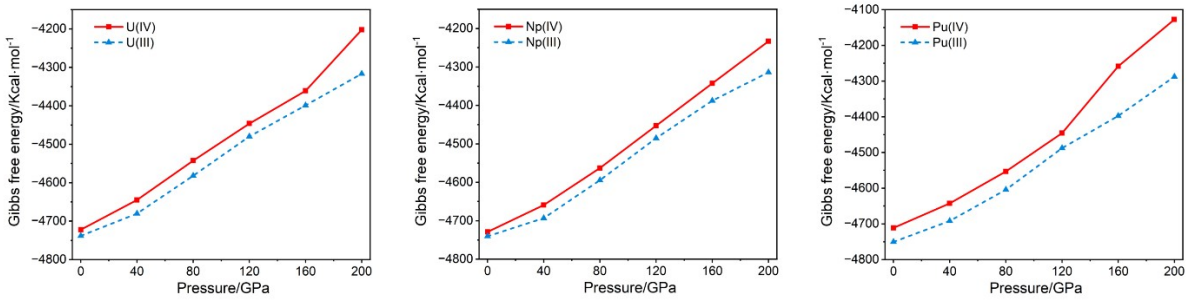

Figure S6. The plot of ΔG versus pressures of molecule models of $An^{III}(COT)_2^-/An^{IV}(COT)_2$.

7. High-pressure MD simulations.

Because classical molecular dynamics generally cannot well describe bond breaking and bond formation processes, particularly in actinide-ligand systems, all dynamical simulations were carried out using *ab initio* molecular dynamics (AIMD) as implemented in VASP.[17-19] A time step of 0.5 fs was employed at 298 K. Prior to the high-pressure simulations, a short NVT AIMD run of 3 ps at ambient pressure was performed to remove unfavorable contacts and pre-equilibrate the structures. High-pressure AIMD simulations were then conducted in the NPT ensemble with a total simulation time of 15 ps. It is important to note that the AIMD simulations reveal qualitative differences compared to static DFT calculations. While static zero-temperature DFT optimizations indicate the formation of four-membered ring motifs only at very high pressures (around 200 GPa), similar structural motifs are already observed in AIMD simulations at much lower nominal pressures (40 GPa) and can persist over the simulation timescale (Figure S7).

This difference arises from the fundamental distinction between static and dynamical approaches. Static DFT calculations probe thermodynamic stability at 0 K, whereas AIMD simulations are performed at finite temperature and therefore allow the system to overcome energy barriers and access kinetically accessible metastable configurations. In addition, although the target pressure is set to 40 GPa in the NPT ensemble, significant instantaneous fluctuations of both pressure (82 GPa) and temperature (5000 K, Figure S8) occur during the early stages of the simulation. These transient high-pressure and high-temperature conditions effectively accelerate structural evolution and facilitate bond rearrangement processes.

Importantly, this behavior does not contradict our static DFT results. Instead, it highlights that pressure-induced bonding rearrangements are kinetically accessible under realistic finite-temperature conditions at pressures lower than those required to stabilize the same motifs as thermodynamic minima at 0 K. The AIMD results therefore reinforce, rather than weaken, our main conclusion that increasing pressure promotes structural destabilization and bonding reorganization in the $U^{IV}(COT)_2$ system.

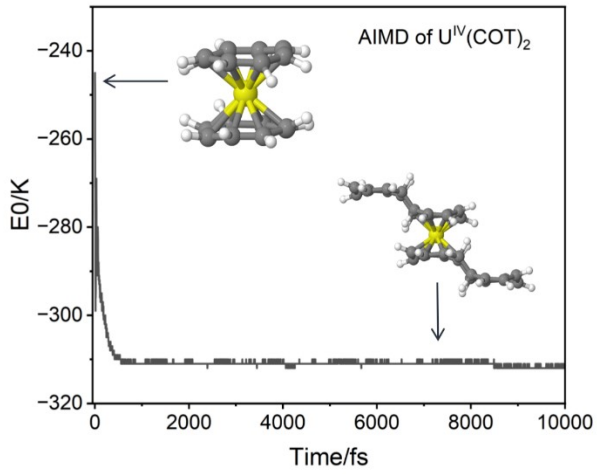

Figure S7. The AIMD plot of total energy E0 versus time of $U^{IV}(COT)_2$ at 40 GPa and the corresponding the corresponding structural evolution of $U^{IV}(COT)_2$.

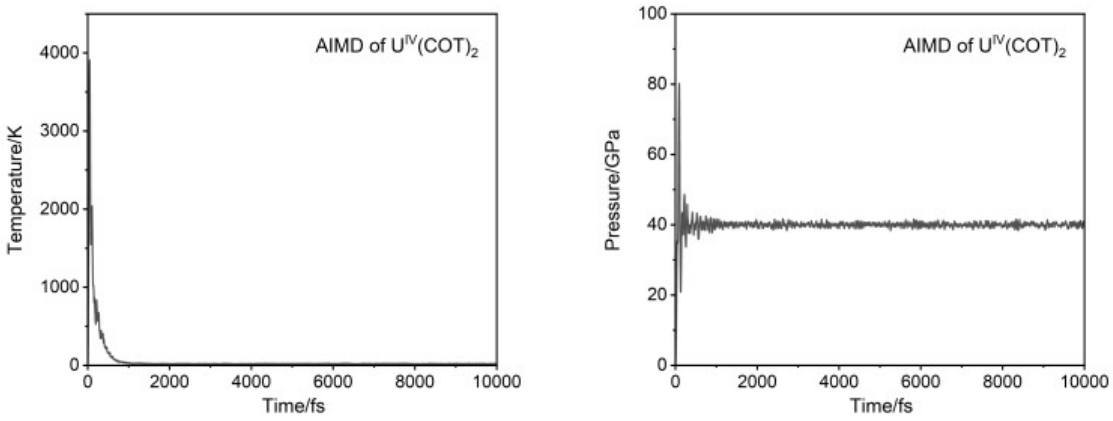

Figure S8. The AIMD plot of pressure and temperature versus time of $U^{IV}(COT)_2$ at 40 GPa.

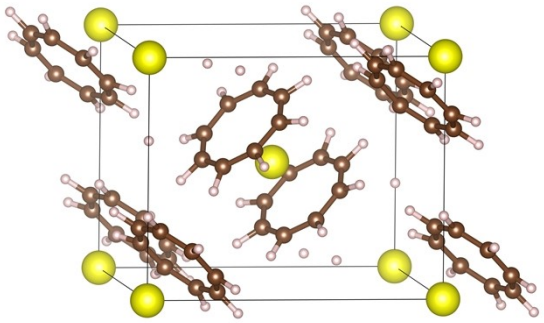

Figure S9. The primitive 1×1×1 unit cell of $U^{IV}(COT)_2$.

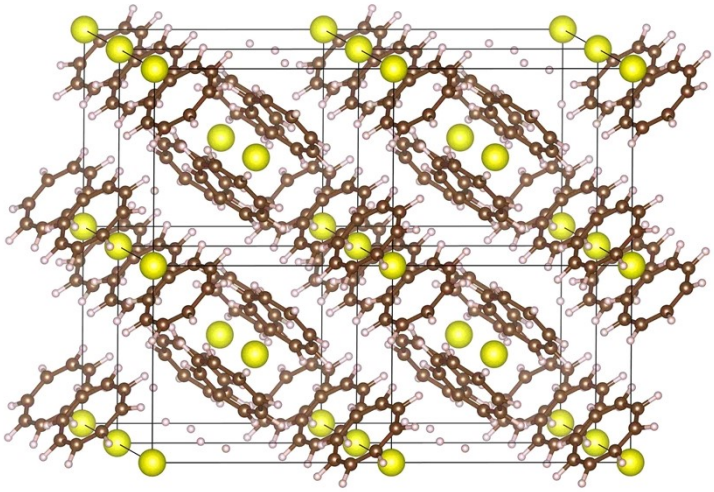

Figure S10. The 2×2×2 supercell of $U^{IV}(COT)_2$.

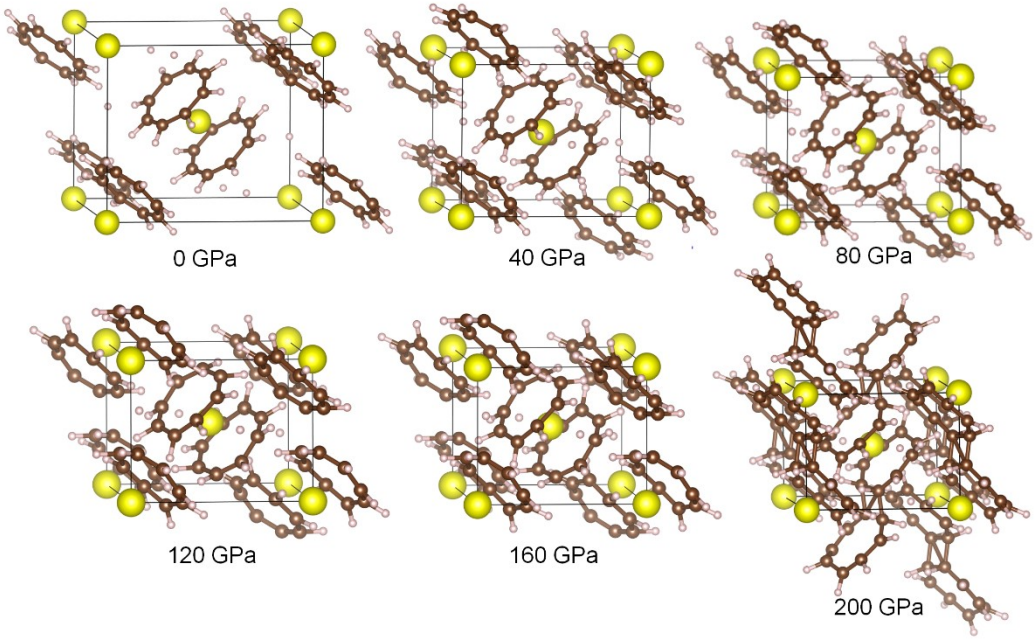

Figure S11. The optimized periodic cells of $U^{IV}(COT)_2$ at different pressures.

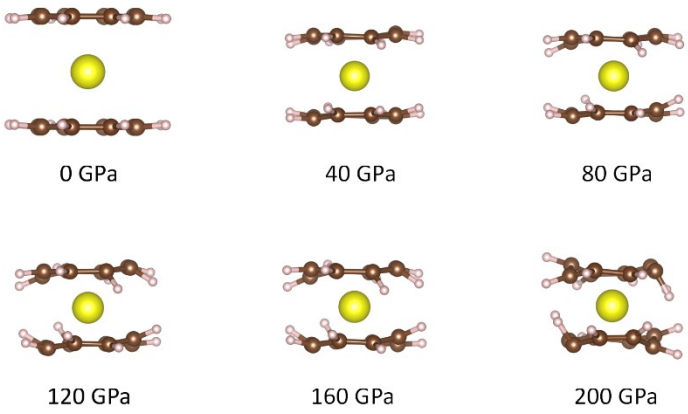

Figure S12. Molecular structures of $U^{IV}(COT)_2$ extracted from the optimized periodic cells at different pressures.

Table S10. Unit cell parameters optimized for $U^{IV}(COT)_2$ at different pressures.

Pressure (GPa)	a (Å)	b (Å)	c (Å)	alpha (degrees)	beta (degrees)	gamma (degrees)	Volume (Å^3 / cell)
0	7.30	8.93	10.79	90.00	99.30	90.00	703.63
40	5.90	7.21	8.87	90.00	97.88	90.00	377.02
80	5.75	6.80	8.09	90.00	98.11	90.00	316.02
120	5.67	6.25	7.93	90.00	98.54	90.00	280.82
160	5.57	6.17	7.52	90.00	99.15	90.00	258.55
200	5.74	5.62	7.41	90.00	100.25	90.00	238.92

Table S11. Unit cell parameters optimized for $Np^{IV}(COT)_2$ at different pressures.

Pressure (GPa)	a (Å)	b (Å)	c (Å)	alpha (degrees)	beta (degrees)	gamma (degrees)	Volume (Å^3 / cell)
0	7.29	8.93	10.79	90.00	99.46	90.00	702.71
40	5.93	7.18	8.88	90.00	98.55	90.00	377.35
80	5.71	6.81	8.15	90.00	98.27	90.00	316.91
120	5.66	6.21	7.97	90.00	98.97	90.00	280.05
160	5.59	6.08	7.54	90.00	99.83	90.00	256.12
200	5.65	5.63	7.49	90.00	100.31	90.00	238.58

Table S12. Unit cell parameters optimized for $Pu^{IV}(COT)_2$ at different pressures.

Pressure (GPa)	a (Å)	b (Å)	c (Å)	alpha (degrees)	beta (degrees)	gamma (degrees)	Volume (Å^3 / cell)
0	7.29	8.95	10.80	90.00	99.29	90.00	704.56
40	5.92	7.16	8.85	90.00	98.72	90.00	374.97
80	5.70	6.86	8.08	90.00	98.28	90.00	316.28
120	5.63	6.50	7.69	90.00	99.05	90.00	281.30
160	5.91	5.64	7.58	90.00	100.35	90.00	252.81
200	5.89	5.52	7.26	90.00	100.64	90.00	236.05

Table S13. Unit cell parameters optimized for $U^{III}(COT)_2^-$ at different pressures.

Pressure (GPa)	a (Å)	b (Å)	c (Å)	alpha (degrees)	beta (degrees)	gamma (degrees)	Volume (Å^3 / cell)
0	8.20	10.11	12.20	90.00	99.09	90.00	1011.61
40	5.96	7.40	9.02	90.00	98.15	90.00	397.78
80	5.78	6.91	8.21	90.00	98.12	90.00	328.06
120	5.73	6.53	7.79	90.00	99.04	90.00	291.42
160	5.61	6.14	7.72	90.00	99.13	90.00	266.02
200	5.51	6.10	7.40	90.00	99.78	90.00	248.75

Table S14. Unit cell parameters optimized for $Np^{III}(COT)_2^-$ at different pressures.

Pressure (GPa)	a (Å)	b (Å)	c (Å)	alpha (degrees)	beta (degrees)	gamma (degrees)	Volume (Å^3 / cell)
0	8.07	9.95	12.01	90.00	99.05	90.00	964.20
40	6.02	7.31	8.94	90.00	98.62	90.00	393.84
80	5.72	6.96	8.29	90.00	97.84	90.00	330.11
120	5.70	6.68	7.66	90.00	99.09	90.00	291.13
160	5.70	6.14	7.58	90.00	99.83	90.00	265.04
200	5.67	5.67	7.67	90.00	99.82	90.00	246.65

Table S15. Unit cell parameters optimized for $Pu^{III}(COT)_2^-$ at different pressures.

Pressure (GPa)	a (Å)	b (Å)	c (Å)	alpha (degrees)	beta (degrees)	gamma (degrees)	Volume (Å^3 / cell)
0	8.44	10.32	12.49	90.00	99.52	90.00	1086.88
40	5.96	7.38	9.03	90.00	98.25	90.00	397.08
80	5.72	6.96	8.29	90.00	97.84	90.00	330.11
120	5.70	6.68	7.66	90.00	99.09	90.00	291.13
160	5.63	6.25	7.57	90.00	99.30	90.00	266.19
200	5.52	6.43	6.99	90.00	101.29	90.00	248.26

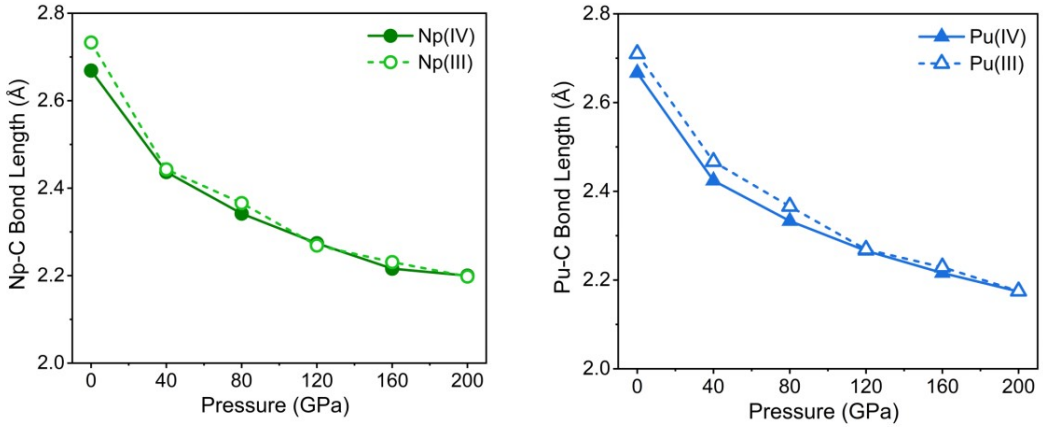

Figure S13. The plot of average $Np^{III/IV}$-C and $Pu^{III/IV}$-C bond lengths at different pressures.

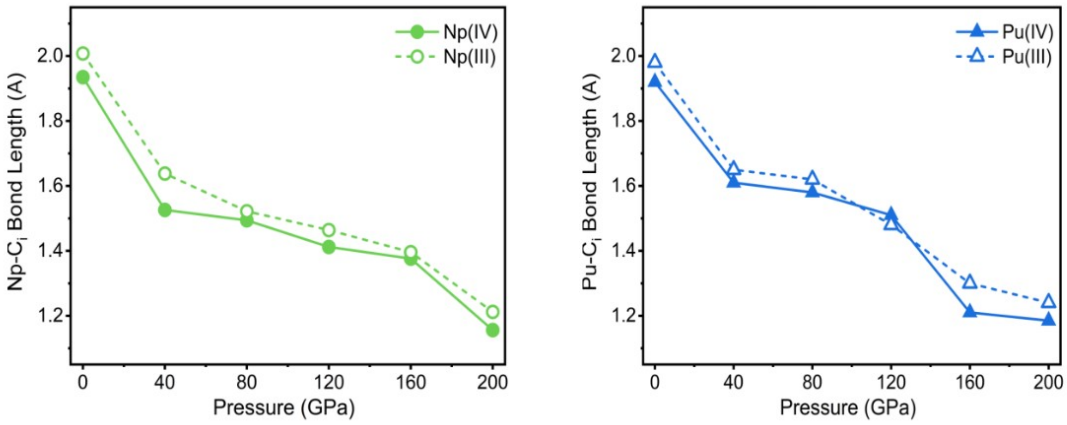

Figure S14. The plot of average $Np^{III/IV}$-C_i and $Pu^{III/IV}$-C_i bond lengths at different pressures where C_i denotes the centroid of the COT ring.

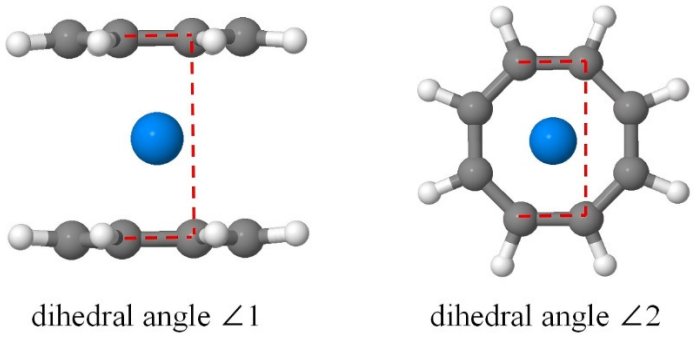

Figure S15. The different dihedral angles in $An^{III}(COT)_2^-$/$An^{IV}(COT)_2$ system.

Table S16. The dihedral angles in $An^{IV}(COT)_2$ system at different pressures (°).

	U(IV)	U(IV)	Np(IV)	Np(IV)	Pu(IV)	Pu(IV)
Pressure/GPa	∠1	∠2	∠1	∠2	∠1	∠2
0	0	0	0	0	0	0
40	1.050	5.380	0.975	4.225	0.950	3.750
80	1.700	5.480	1.625	5.225	1.675	5.175
120	2.550	6.375	2.575	5.925	2.050	5.925
160	2.500	8.075	2.625	8.025	5.450	10.700
200	5.550	9.375	4.950	7.925	6.475	12.525

Table S17. The dihedral angles in $An^{III}(COT)_2^-$ system at different pressures (°).

	U(III)	U(III)	Np(III)	Np(III)	Pu(III)	Pu(III)
Pressure/GPa	∠1	∠2	∠1	∠2	∠1	∠2
0	0	0	0	0	0	0
40	0.875	4.100	0.850	4.575	0.875	4.050
80	1.625	4.750	1.475	4.775	1.575	5.400
120	1.725	6.525	1.650	5.950	1.725	5.950
160	2.850	8.450	2.575	8.425	2.275	7.600
200	2.650	9.000	4.850	8.200	2.625	5.200

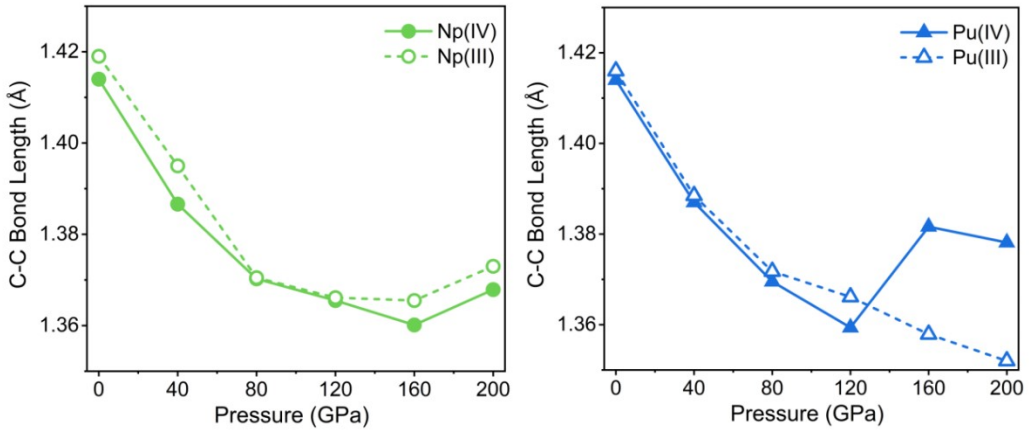

Figure S16. The plot of average C-C bond lengths in Np/Pu-COT systems at different pressures.

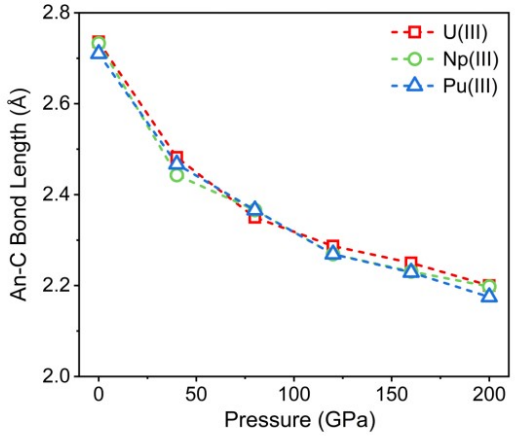

Figure S17. The plot of average An^{III}-C bond lengths in An-COT systems at different pressures.

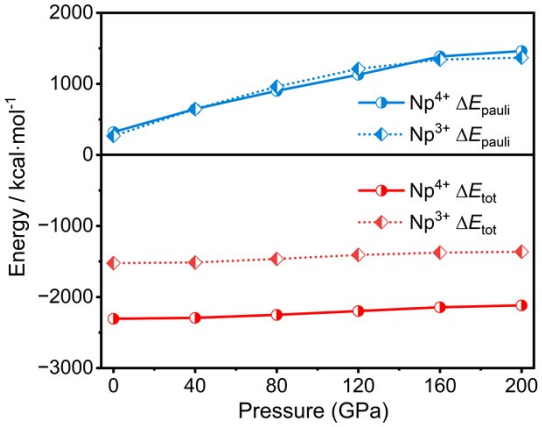

Figure S18. The results of EDA analysis for fragments $Np^{3+/4+}$ and $2COT_2^-$ at different pressures.

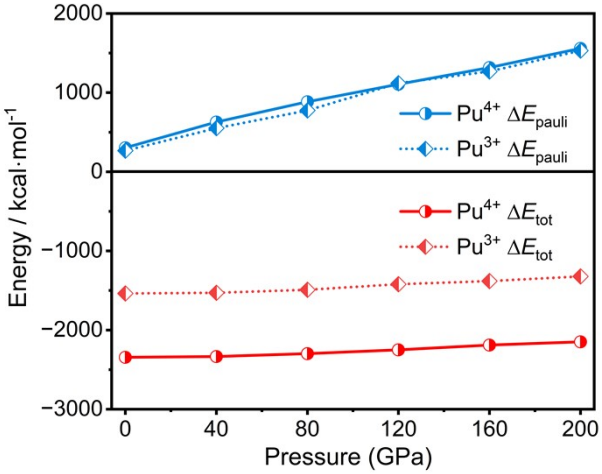

Figure S19. The results of EDA analysis for fragments $Pu^{3+/4+}$ and $2COT_2^-$ at different pressures.

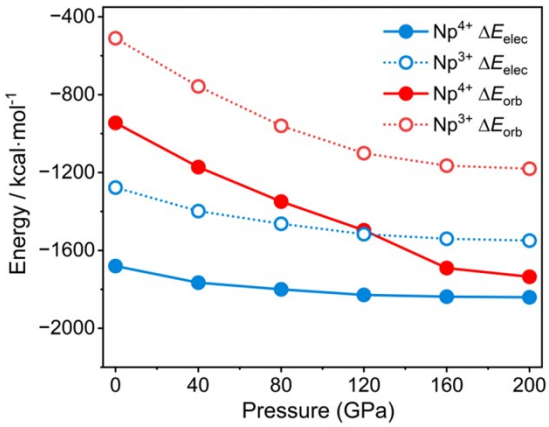

Figure S20. The results of EDA analysis for fragments $Np^{3+/4+}$ and $2COT_2^-$ at different pressures.

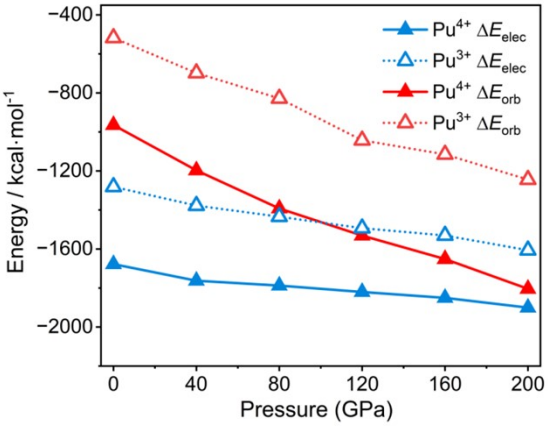

Figure S21. The results of EDA analysis for fragments $Pu^{3+/4+}$ and $2COT_2^-$ at different pressures.

Table S18. The results of EDA analysis of $U^{IV}(COT)_2$ for neutral fragments U and 2COT at different pressures (kcal·mol^{-1}).

U(VI)	E_{pauli}	E_{elect}	E_{orb}	E_{disp}	E_{tot}
0	905.78	-540.29	-641.88	-4.23	-280.63
40	1535.81	-839.52	-904.34	-3.65	-211.70
80	1936.01	-1014.84	-1050.81	-3.26	-132.90
120	2201.98	-1140.06	-1145.46	-3.03	-86.57
160	2392.00	-1207.77	-1215.30	-2.89	-33.98
200	2667.63	-1324.16	-1333.03	-2.78	7.64

Table S19. The results of EDA analysis of $U^{III}(COT)_2$ for neutral fragments U and 2COT at different pressures (kcal·mol^{-1}).

U(III)	E_{pauli}	E_{elect}	E_{orb}	E_{disp}	E_{tot}
0	818.33	-494.38	-620.68	-4.29	-301.02
40	1426.57	-790.32	-876.08	-3.76	-243.60
80	1879.36	-978.79	-1043.41	-3.26	-146.11
120	2193.90	-1126.05	-1164.37	-3.01	-99.53
160	2354.63	-1188.12	-1229.06	-2.88	-65.43
200	2533.38	-1267.66	-1277.85	-2.79	-14.95

Table S20. The total energy of different states of $An^{IV}(COT)_2$ (An = U, Np, Pu) at different pressures (kcal·mol^{-1}).

	$U^{IV}(COT)_2$			$Np^{IV}(COT)_2$			$Pu^{IV}(COT)_2$		
Pressure/GPa	singlet	triplet	Δ*E*	doublet	quartet	Δ*E*	triplet	quintet	Δ*E*
0	-4852.09	-4859.40	7.31	-4851.59	-4866.13	14.54	-4825.22	-4848.52	23.30
40	-4786.39	-4789.94	3.55	-4792.67	-4803.76	11.09	-4769.86	-4787.69	17.83
80	-4687.66	-4688.18	0.52	-4702.47	-4709.97	7.50	-4684.84	-4700.18	15.34
120	-4592.32	-4590.18	-2.14	-4594.95	-4600.60	5.65	-4582.02	-4595.11	13.09
160	-4507.75	-4502.95	-4.80	-4489.05	-4491.34	2.29	-4404.72	-4407.76	3.04
200	-4357.54	-4348.77	-8.77	-4379.43	-4378.67	-0.76	-4275.31	-4270.27	-5.04

Table S21 The total energy of different states of $An^{III}(COT)_2^-$ (An = U, Np, Pu) at different pressures (kcal·mol^{-1}).

	$U^{III}(COT)_2^-$			$Np^{III}(COT)_2^-$			$Pu^{III}(COT)_2^-$		
Pressure/GPa	doublet	quartet	Δ*E*	triplet	quintet	Δ*E*	quartet	sextet	Δ*E*
0	-4860.56	-4872.17	11.61	-4875.79	-4892.98	17.19	-4859.24	-4886.08	26.84
40	-4813.84	-4819.89	6.05	-4823.14	-4834.91	11.77	-4812.22	-4834.01	21.79
80	-4720.89	-4717.87	-3.02	-4730.23	-4738.03	7.80	-4737.78	-4748.93	11.15
120	-4621.37	-4615.01	-6.36	-4627.89	-4629.77	1.88	-4632.33	-4625.79	-6.54
160	-4541.68	-4530.61	-11.07	-4539.04	-4534.03	-5.01	-4543.78	-4530.42	-13.36
200	-4460.40	-4445.61	-14.79	-4457.83	-4445.92	-11.91	-4434.20	-4415.91	-18.29

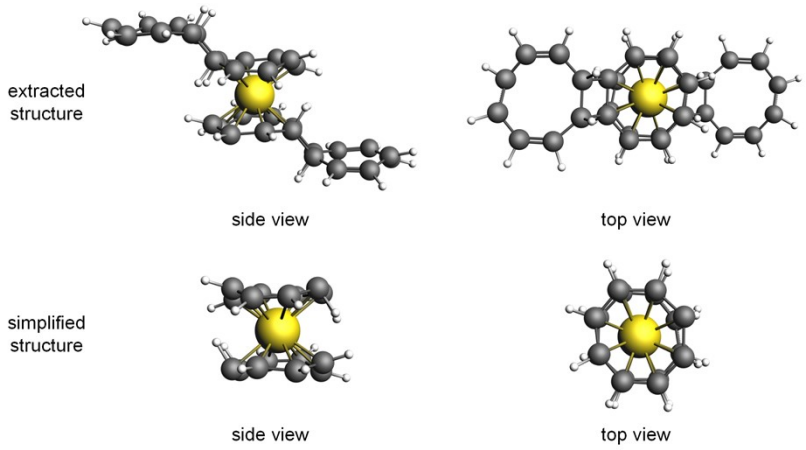

Figure S22. The simplified structure of $U^{IV}(COT)_2$ in CASSCF calculations and extracted structure including inter-ring C-C bond framework of $U^{IV}(COT)_2$ at 200 GPa.

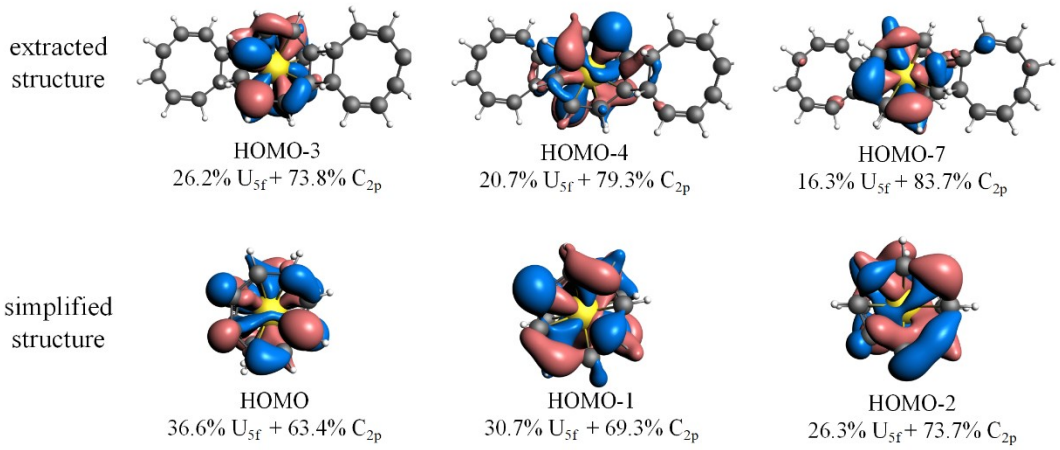

Figure S23. The selected frontier Kohn-Sham valence orbitals of extracted and simplified structures of $U^{IV}(COT)_2$ at 160 GPa (isosurface = 0.03 a.u.).

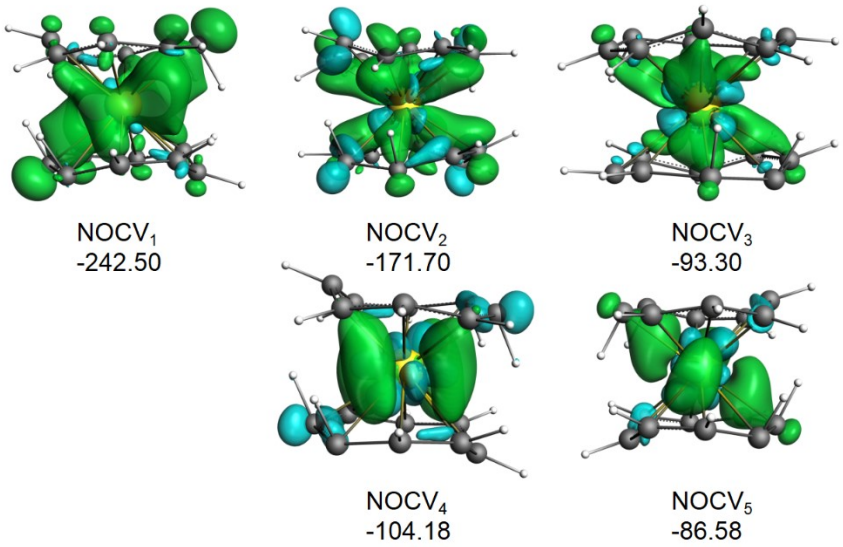

Figure S24. The NOCV analysis for fragments U^{4+} and $2COT_2^-$ at 200 GPa (kcal·mol^{-1}) where the charge flows from C 2p (azure) to U 5f/6d orbitals (green).

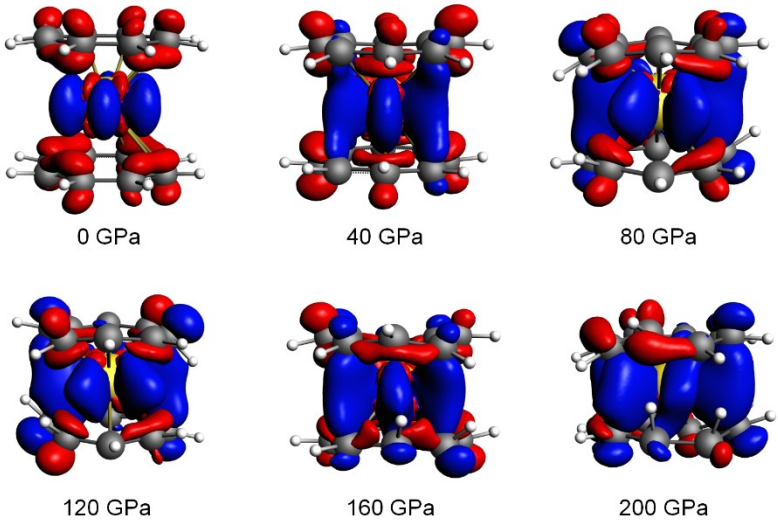

Figure S25. The deformation density $\Delta\rho$ between fragments U^{4+} and $2COT_2^-$ at different pressures based on the ETA-NOCV analysis where electron flows from the red to blue region.

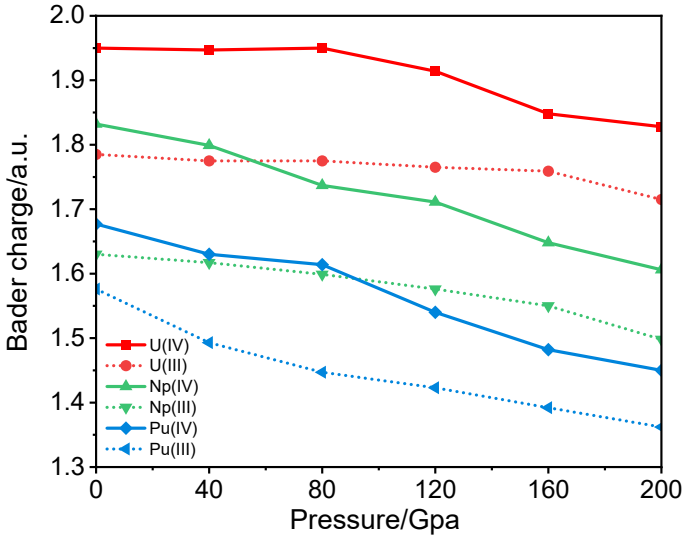

Figure S26. The calculated Bader charge of actinide mental center in $An^{III}(COT)_2^-$/$An^{IV}(COT)_2$ systems at different pressures.

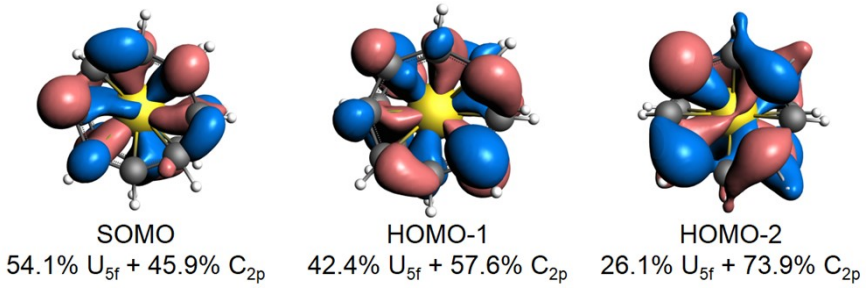

Figure S27. The frontier Kohn-Sham ϕ valence orbitals of $U^{III}(COT)_2^-$ at 200 GPa (isosurface = 0.03 a.u.)

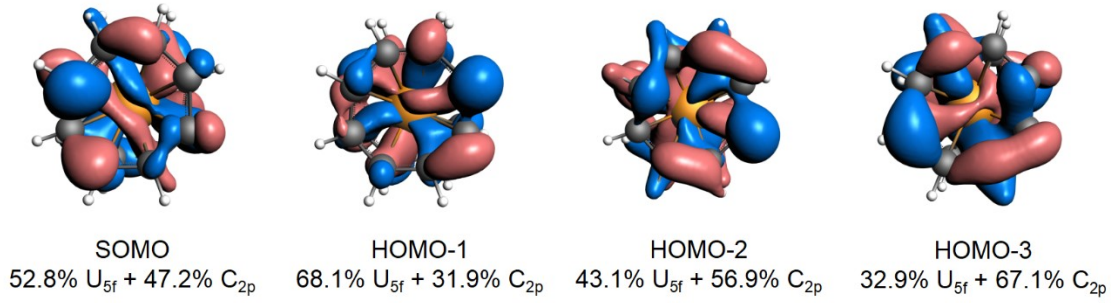

Figure S28. The frontier Kohn-Sham ϕ valence orbitals of $Np^{IV}(COT)_2$ at 200 GPa (isosurface = 0.03 a.u.)

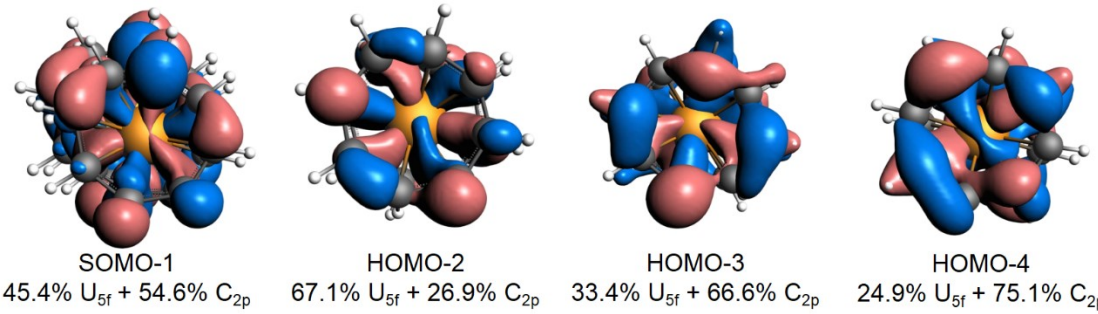

Figure S29. The frontier Kohn-Sham ϕ valence orbitals of $Np^{III}(COT)_2^-$ at 200 GPa (isosurface = 0.03 a.u.)

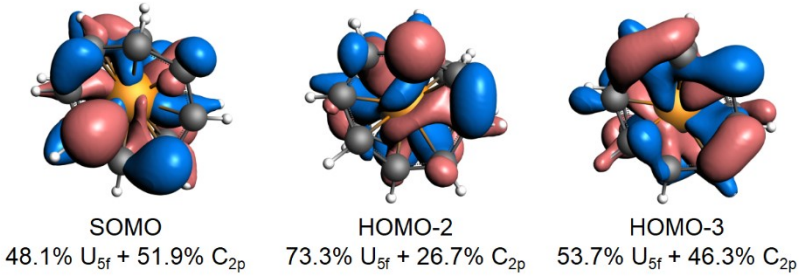

Figure S30. The frontier Kohn-Sham ϕ valence orbitals of $Pu^{IV}(COT)_2$ at 200 GPa (isosurface = 0.03 a.u.)

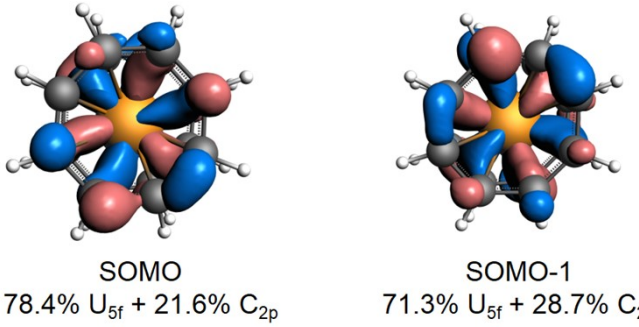

Figure S31. The frontier Kohn-Sham ϕ valence orbitals of $Pu^{III}(COT)_2^-$ at 200 GPa (isosurface = 0.03 a.u.)

Appendix

Appendix 1. The excised cartesian coordinates of $U^{IV}(COT)_2$ at 0 and 200 GPa.

0 GPa				200 GPa			
U	2.791640	4.466532	5.318261	U	-1.831438	5.501348	-6.782751
C	1.272304	4.622294	3.105705	C	-0.650842	5.078763	-5.073317
C	4.310975	4.310770	7.530818	H	-0.225908	4.185640	-4.742843
C	0.527613	5.282809	4.108617	H	1.167711	5.392749	-5.905087
C	5.055667	3.650255	6.527906	H	-0.600177	3.480194	-6.042328
C	0.817439	6.258943	5.091268	H	-2.050525	5.118772	-3.576217
C	4.765841	2.674120	5.545255	C	-1.848525	5.527368	-4.520155
C	1.970055	6.999841	5.449988	C	0.210531	5.791780	-5.815330
C	3.613225	1.933223	5.186535	C	-3.023778	5.925986	-5.024836
C	3.299981	7.082261	4.973972	C	-0.060745	6.670481	-6.823934
C	2.283299	1.850802	5.662551	H	-3.832893	5.334296	-4.753254
C	4.040088	6.436045	3.958369	C	-3.319503	6.874540	-5.858558
C	1.543191	2.497018	6.678154	C	-1.146473	7.532425	-7.156724
C	3.760116	5.424831	3.009266	H	0.804171	6.886803	-7.387821
C	1.823164	3.508232	7.627257	C	-1.161244	3.327420	-6.977668
C	2.613717	4.671144	2.658753	H	-4.312951	6.979159	-6.066805
C	2.969563	4.261919	7.977770	C	-2.501632	7.675275	-6.587834
H	0.706765	3.820397	2.625622	H	-1.375681	7.234628	-8.194069
H	4.876514	5.112666	8.010901	C	-2.516403	3.470271	-6.408778
H	-0.477416	4.867030	4.218751	C	-0.343373	4.128155	-7.706944
H	6.060696	4.066034	6.417772	H	-3.062699	7.522501	-7.523174
H	-0.012740	6.419823	5.784761	C	-3.602131	4.332214	-6.741568
H	5.596020	2.513241	4.851762	H	-2.287195	3.768067	-5.371433
H	1.822549	7.596071	6.353066	C	-0.639098	5.076710	-8.540666
H	3.760731	1.336992	4.283457	H	0.650074	4.023537	-7.498697
H	3.920490	7.725957	5.601412	C	-3.873408	5.210915	-7.750172
H	1.662789	1.207106	5.035111	H	-4.467048	4.115893	-6.177681
H	5.099931	6.702536	3.981430	C	-1.814351	5.475327	-9.045347
H	0.483349	2.230527	6.655093	H	0.170016	5.668400	-8.812248
H	4.656429	5.086699	2.482774	H	-4.830588	5.609947	-7.660415
H	0.926850	3.846364	8.153749	C	-3.012034	5.923932	-8.492185
H	2.828406	3.891724	1.923705	H	-1.612351	5.883924	-9.989285
H	2.754874	5.041339	8.712818	H	-3.436968	6.817055	-8.822659

Appendix 2. The excised cartesian coordinates of $U^{III}(COT)_2^-$ at 0 and 200 GPa.

0 GPa				200 GPa			
U	3.146315	5.054002	6.018353	U	2.117803	3.051777	3.649756
C	1.606693	5.250350	3.764714	C	0.869894	2.549851	1.946045
C	4.685937	4.857654	8.271993	C	3.365712	3.553704	5.353466
C	0.856775	5.905945	4.773208	C	0.101783	3.379442	2.688350
C	5.435855	4.202058	7.263499	C	4.133823	2.724113	4.611161
C	1.148576	6.895848	5.746993	C	0.371139	4.282661	3.705184
C	5.144054	3.212155	6.289714	C	3.864467	1.820894	3.594327
C	2.295789	7.653793	6.095341	C	1.475329	5.086888	4.026672
C	3.996841	2.454211	5.941366	C	2.760277	1.016667	3.272839
C	3.633426	7.716334	5.628002	C	2.741281	5.239897	3.474954
C	2.659204	2.391669	6.408705	C	1.494325	0.863658	3.824557
C	4.383645	7.061006	4.619378	C	3.433267	4.580415	2.554050
C	1.908985	3.046997	7.417329	C	0.802339	1.523140	4.745461
C	4.097504	6.053653	3.661947	C	3.151981	3.515970	1.824535
C	2.195126	4.054351	8.374760	C	1.083625	2.587585	5.474976
C	2.945083	5.309992	3.299705	C	2.071545	2.866031	1.409620
C	3.347547	4.798012	8.737002	C	2.164060	3.237524	5.889892
H	1.032814	4.464709	3.263379	H	0.500042	1.596740	1.759422
H	5.259816	5.643295	8.773328	H	3.735564	4.506815	5.540089
H	0.163748	5.519181	4.859347	H	-0.553005	4.512976	4.178423
H	6.456377	4.588823	7.177360	H	4.788611	1.590579	3.121088
H	0.304822	7.082434	6.419824	H	1.694354	5.092571	5.085708
H	5.987807	3.025570	5.616883	H	2.541252	1.010984	2.213803
H	2.129008	8.293498	6.967159	H	3.410335	5.406928	4.276791
H	4.163622	1.814506	5.069548	H	0.825271	0.696627	3.022720
H	4.249586	8.386311	6.235994	H	4.452854	4.721556	2.564082
H	2.043044	1.721693	5.800713	H	-0.217248	1.381998	4.735429
H	5.438419	7.353952	4.619160	H	3.977430	3.109677	1.346459
H	0.854210	2.754052	7.417547	H	0.258176	2.993878	5.953052
H	4.988270	5.742604	3.105751	H	2.317189	2.479789	0.466594
H	1.304360	4.365400	8.930956	H	1.918417	3.623766	6.832917
H	3.148920	4.564142	2.525445	H	-0.891559	3.050550	2.773846
H	3.143710	5.543862	9.511262	H	5.127165	3.053005	4.525665

Appendix 3. The excised cartesian coordinates of $Np^{IV}(COT)_2$ at 0 and 200 GPa.

0 GPa				200 GPa			
Np	2.779287	4.467191	5.312000	Np	-4.642306	4.442908	-6.852089
C	1.269298	4.604372	3.115949	C	-3.437006	3.988234	-5.143049
C	4.289276	4.330010	7.508050	C	-4.634284	4.372729	-4.604829
C	0.527971	5.263204	4.124914	H	-3.005070	3.121701	-4.763600
C	5.030603	3.671177	6.499086	H	-1.646160	4.344939	-5.989562
C	0.808132	6.254577	5.094823	H	-3.375553	2.429015	-6.106514
C	4.750442	2.679804	5.529177	H	-4.860329	3.992901	-3.654098
C	1.960226	6.994886	5.450538	C	-2.617625	4.713909	-5.911085
C	3.598348	1.939495	5.173462	C	-5.770556	4.884766	-5.058471
C	3.294194	7.066651	4.986506	C	-2.900634	5.605307	-6.915684
C	2.264380	1.867731	5.637493	H	-6.600549	4.334346	-4.756867
C	4.034026	6.413774	3.972757	C	-6.086859	5.835822	-5.877341
C	1.524548	2.520607	6.651242	C	-3.976522	6.485908	-7.224211
C	3.752620	5.417903	3.008394	H	-2.014139	5.855989	-7.440063
C	1.805954	3.516479	7.615606	C	-3.948142	2.263969	-7.027521
C	2.606051	4.666703	2.659090	H	-7.099286	5.907775	-5.986138
C	2.952523	4.267679	7.964910	C	-5.336470	6.621847	-6.676657
H	0.703502	3.803684	2.635186	H	-4.207362	6.241103	-8.268520
H	4.855072	5.130697	7.988814	C	-5.308090	2.399907	-6.479967
H	0.474627	4.842789	4.238812	C	-3.197753	3.049994	-7.826837
H	6.033201	4.091593	6.385187	H	-5.909059	6.456800	-7.597664
H	0.025799	6.424372	5.781039	C	-6.383978	3.280509	-6.788494
H	5.584373	2.510010	4.842961	H	-5.077250	2.644712	-5.435658
H	1.811307	7.594881	6.351293	C	-3.514056	4.001049	-8.645707
H	3.747267	1.339501	4.272707	H	-2.185326	2.978041	-7.718040
H	3.914036	7.712094	5.612210	H	-7.270473	3.029826	-6.264115
H	1.644538	1.222287	5.011790	C	-6.666987	4.171906	-7.793093
H	5.094623	6.676837	3.999192	C	-4.650328	4.513086	-9.099349
H	0.463951	2.257545	6.624808	H	-2.684063	4.551470	-8.947311
H	4.646133	5.089219	2.472161	H	-7.638452	4.540877	-7.714616
H	0.912441	3.845163	8.151839	C	-5.847606	4.897582	-8.561129
H	2.820380	3.890041	1.920668	H	-4.424283	4.892914	-10.050080
H	2.738194	5.044341	8.703332	H	-6.279542	5.764114	-8.940578

Appendix 4. The excised cartesian coordinates of $Np^{III}(COT)_2^-$ at 0 and 200 GPa.

0 GPa			200 GPa		
Np	3.097772	4.975049	5.924957	Np	2.176038	2.833786	3.782807
C	1.559165	5.162358	3.672460	C	0.950228	2.412680	2.028301
C	4.636380	4.787741	8.177454	C	3.401848	3.254892	5.537313
C	0.812781	5.822553	4.683335	C	0.141309	3.132229	2.822223
C	5.382764	4.127546	7.166579	C	4.210766	2.535343	4.743391
C	1.098996	6.818636	5.652384	C	0.431253	4.010009	3.847927
C	5.096549	3.131463	6.197530	C	3.920822	1.657563	3.717687
C	2.250016	7.567781	6.007317	C	1.503431	4.907530	4.145389
C	3.945528	2.382318	5.842597	C	2.848644	0.760042	3.420225
C	3.589161	7.635280	5.542264	C	2.896460	5.014255	3.640307
C	2.606384	2.314819	6.307650	C	1.455616	0.653317	3.925307
C	4.335345	6.976555	4.530268	C	3.617008	4.243374	2.789573
C	1.860199	2.973544	7.319646	C	0.735067	1.424198	4.776041
C	4.050285	5.975330	3.566357	C	3.293901	3.292923	1.962257
C	2.145259	3.974769	8.283557	C	1.058174	2.374649	5.603357
C	2.899789	5.224704	3.211679	C	2.166219	2.751521	1.522174
C	3.295755	4.725395	8.638235	C	2.185856	2.916051	6.043440
H	0.978468	4.392435	3.155985	H	0.491505	1.573198	1.607839
H	5.217076	5.557664	8.693929	H	3.860571	4.094374	5.957775
H	-0.211419	5.443298	4.763408	H	-0.450058	4.294219	4.371909
H	6.406964	4.506801	7.086506	H	4.802133	1.373353	3.193705
H	0.247219	7.021886	6.310367	H	1.706954	4.702181	5.196524
H	5.948325	2.928213	5.539547	H	2.645122	0.965391	2.369090
H	2.079611	8.214410	6.873659	H	3.443110	4.810449	4.556516
H	4.115934	1.735689	4.976255	H	0.908965	0.857123	3.009098
H	4.199928	8.322081	6.135873	H	4.635536	4.299958	2.893033
H	1.995616	1.628018	5.714041	H	-0.283460	1.367614	4.672581
H	5.388490	7.276723	4.522438	H	4.119453	2.719773	1.661304
H	0.807055	2.673376	7.327476	H	0.232623	2.947799	5.904310
H	4.936652	5.682263	2.993431	H	2.371906	2.389116	0.555744
H	1.258893	4.267836	8.856483	H	1.980170	3.278456	7.009870
H	3.102662	4.485022	2.430952	H	-0.816869	2.723916	2.920950
H	3.092882	5.465077	9.418962	H	5.168944	2.943656	4.644664

Appendix 5. The excised cartesian coordinates of $Pu^{III}(COT)_2$ at 0 and 200 GPa.

0 GPa				200 GPa			
Pu	2.786621	4.475041	5.322667	Pu	5.794989	-1.302230	12.309159
C	1.276295	4.610978	3.128088	C	4.674153	-0.988923	10.623088
C	4.296947	4.339104	7.517246	H	4.206998	-0.085117	10.345906
C	0.533247	5.270324	4.134095	H	2.869564	-1.157049	11.460824
C	5.039995	3.679758	6.511239	H	4.690331	0.811602	11.549181
C	0.818292	6.258945	5.106745	H	6.065411	-0.987523	9.194518
C	4.754950	2.691137	5.538590	C	3.758082	-1.672993	11.333608
C	1.967579	7.002546	5.463598	C	5.906919	-1.480288	10.118583
C	3.605663	1.947535	5.181737	C	4.024781	-2.528458	12.332650
C	3.301062	7.072999	4.997249	C	7.129621	-1.666064	10.690971
C	2.272181	1.877083	5.648085	H	3.289095	-2.611188	13.076928
C	4.041274	6.423176	3.983009	C	5.115114	-3.303961	12.711704
C	1.531968	2.526906	6.662326	C	7.404266	-2.587890	11.591795
C	3.757844	5.422406	3.022822	H	7.843812	-0.981980	10.385422
C	1.815398	3.527676	7.622512	C	5.146615	0.825682	12.546081
C	2.612883	4.671052	2.669717	H	5.337702	-2.974575	13.766745
C	2.960359	4.279030	7.975617	C	6.443364	-3.430142	12.072235
H	0.708884	3.813492	2.643262	H	8.274225	-2.684465	12.128092
H	4.864358	5.136590	8.002073	C	4.185712	-0.016570	13.026522
H	0.475245	4.863001	4.238274	C	6.474864	0.699501	11.906612
H	6.048487	4.087081	6.407060	H	6.899647	-3.416062	13.069135
H	0.018200	6.433176	5.789106	H	3.315753	0.080005	12.490225
H	5.591442	2.516906	4.856229	C	4.460358	-0.938396	13.927345
H	1.814174	7.612053	6.356617	H	6.252276	0.370115	10.851572
H	3.759068	1.338029	4.288718	C	7.565197	-0.076002	12.285668
H	3.919871	7.722999	5.619757	H	3.746167	-1.622480	14.232894
H	1.653371	1.227082	5.025578	C	5.683060	-1.124172	14.499733
H	5.098735	6.697554	3.997514	H	8.300883	0.006728	11.541389
H	0.474508	2.252527	6.647820	C	7.831897	-0.931467	13.284709
H	4.650597	5.097418	2.482605	C	6.915825	-1.615537	13.995228
H	0.922645	3.852664	8.162730	H	5.524568	-1.616937	15.423798
H	2.824821	3.902898	1.922460	H	8.720414	-1.447411	13.157493
H	2.748421	5.047184	8.722874	H	7.382981	-2.519343	14.272410

Appendix 6. The excised cartesian coordinates of $Pu^{III}(COT)_2^-$ at 0 and 200 GPa.

0 GPa				200 GPa		
Pu	3.213930	5.159287	6.142492	Pu	2.215093	3.337897	3.796496
C	1.682347	5.326135	3.910816	C	0.901343	2.897731	2.029147
C	4.745514	4.992439	8.374168	C	3.528842	3.778064	5.563845
C	0.939034	5.985612	4.920011	C	0.160177	3.720816	2.817552
C	5.488826	4.332962	7.364973	C	4.270008	2.954978	4.775440
C	1.225020	6.982515	5.885266	C	0.470855	4.677310	3.777752
C	5.202841	3.336059	6.399718	C	3.959331	1.998484	3.815240
C	2.373513	7.732334	6.239457	C	1.611891	5.412418	4.147770
C	4.054347	2.586240	6.045528	C	2.818295	1.263377	3.445222
C	3.710539	7.797175	5.777318	C	2.873479	5.553804	3.626810
C	2.717322	2.521399	6.507666	C	1.556706	1.121990	3.966182
C	4.454051	7.138212	4.767704	C	3.535957	4.923468	2.647281
C	1.973810	3.180362	7.517281	C	0.894229	1.752326	4.945711
C	4.167621	6.140803	3.803015	C	3.216898	3.868935	1.861171
C	2.260240	4.177771	8.481969	C	1.213288	2.806859	5.731821
C	3.019263	5.390804	3.448624	C	2.139663	3.138524	1.518783
C	3.408598	4.927770	8.836360	C	2.290522	3.537270	6.074209
H	1.108076	4.540828	3.410860	H	0.503759	1.938366	1.850695
H	5.319784	5.777746	8.874124	H	3.926426	4.737428	5.742297
H	-0.076878	5.589860	5.016763	H	-0.406519	4.903316	4.349438
H	6.504739	4.728714	7.268221	H	4.836704	1.772479	3.243554
H	0.379545	7.172957	6.553644	H	1.695438	5.712405	5.161222
H	6.048316	3.145617	5.731340	H	2.734748	0.963389	2.431770
H	2.206715	8.365057	7.116188	H	3.545710	6.029391	4.289910
H	4.221145	1.953517	5.168796	H	0.884476	0.646404	3.303082
H	4.327194	8.466888	6.383812	H	4.559616	5.134101	2.585009
H	2.100667	1.851686	5.901173	H	-0.129431	1.541693	5.007983
H	5.511661	7.419626	4.775752	H	4.044076	3.445655	1.363801
H	0.916199	2.898948	7.509232	H	0.386110	3.230139	6.229191
H	5.056718	5.834383	3.243065	H	2.393424	2.579021	0.662696
H	1.371143	4.484191	9.041919	H	2.036761	4.096774	6.930296
H	3.227547	4.640748	2.679838	H	-0.833788	3.375766	2.927099
H	3.200314	5.677826	9.605146	H	5.263974	3.300028	4.665893

References:

(1) John P. Perdew, K. B., Matthias Ernzerhof. Generalized gradient approximation made simple. *Phys. Rev. Lett.,* **1996**, *77*, 3865-3868.

(2) Sperling, J. M.; Warzecha, E. J.; Celis-Barros, C.; Sergentu, D.-C.; Wang, X.; Klamm, B. E.; Windorff, C. J.; Gaiser, A. N.; White, F. D.; Beery, D. A.; et al. Compression of curium pyrrolidine-dithiocarbamate enhances covalency. *Nature* **2020**, *583*, 396-399.

(3) Bai, Z.; Redington, M.; Haldar, S.; Beck, N. B.; Sperling, J. M.; Scheibe, B.; Brannon, J. P.; Zurek, E.; Gagliardi, L.; Albrecht, T. E. High-pressure effects on an octa-hydrated curium complex: An experimental and theoretical investigation. *J. Am. Chem. Soc.,* **2025**. *147*, 6137-6148.

(4) Handy, N. C.; Cohen, A. J. A dynamical correlation functional. *J. Chem. Phys.,* **2002**, *116*, 5411-5418.

(5) Adamo, C.; Barone, V. Toward reliable density functional methods without adjustable parameters: The PBE0 model. *J. Chem. Phys.,* **1999**, *110*, 6158-6170.

(6) Biczysko M.; Scalmani G.; Bloino J.; Barone V.; Harmonic and anharmonic vibrational frequency calculations with the double-hybrid B2PLYP method: analytic second derivatives and benchmark studies, *J. Chem. Theor. Comput.,* **2010**, 6, 2115-2125.

(7) Yanai T.; Tew D. P.; Handy N. C. A new hybrid exchange–correlation functional using the Coulomb-attenuating method (CAM-B3LYP). *Chem. Phys. Lett.,* **2004**, 393, 51-57.

(8) Iikura H.; Tsuneda T.; Yanai T.; Hirao K.; J. *Chem. Phys.,* **2001**, 115, 3540-3544.

(9) Van Lenthe, E.; Van Leeuwen, R.; Baerends, E. J.; Snijders, J. G. Relativistic regular two-component Hamiltonians. *Int. Quantum Chem.,* **1996**, *57*, 281-293.

(10) Iliaš, M.; Saue, T. An infinite-order two-component relativistic Hamiltonian by a simple one-step transformation. *J. Chem. Phys.,* **2007**, *126*, 064102.

(11) Liu, W.; Peng, D. Exact two-component Hamiltonians revisited. *J. Chem. Phys.,* **2009**, *131*, 031104.

(12) Neese, F.; Wennmohs, F.; Becker, U.; Riplinger, C. The ORCA quantum chemistry program package. *J. Chem. Phys.,* **2020**, *152*. 224108.

(13) Moritz, A.; Cao, X.; Dolg, M. Quasirelativistic energy-consistent 5f-in-core pseudopotentials for divalent and tetravalent actinide elements. *Theor. Chem. Acc.,* **2007**, *118*, 845-854.

(14) Bergner, A.; Dolg, M.; Küchle, W.; Stoll, H.; Preuß, H. *Ab initio* energy-adjusted pseudopotentials for elements of groups 13-17. *Mol. Phys.,* **1993**, *80*, 1431-1441.

(15) Wolf, A.; Reiher, M.; Hess, B. A. The generalized Douglas-Kroll transformation. *J. Chem. Phys.,* **2002**, *117*, 9215-9226.

(16) Roos, B. O.; Malmqvist, P. Å. Relativistic quantum chemistry: the multiconfigurational approach. *Phys. Chem. Chem. Phys.,* **2004**, *6*, 2919-2927.

(17) Malmqvist, P. Å.; Roos, B. O.; Schimmelpfennig, B. The restricted active space (RAS) state interaction approach with spin-orbit coupling. *Chem. Phys. Lett.,* **2002**, *357*, 230-240.

(18) P. J. Knowles and H. J. Werner, An efficient second-order MC SCF method for long configuration expansions. *Chem. Phys. Lett.*, **1985**, 115, 259-267.

(19) H. J. Werner, Third-order multireference perturbation theory The CASPT3 method. *Mol. Phys.,* **1996**, 89, 645-661.

(20) T. Shiozaki, W. Gyorffy, P. Celani and H. J. Werner, Communication: Extended multi-state complete active space second-order perturbation theory: Energy and nuclear gradients. *J. Chem. Phys.,* **2011**, 135, 081106.

(21) Baroni, S.; Giannozzi, P.; Testa, A. Green's-function approach to linear response in solids. *Phys. Rev. Lett.,* **1987**, *58*, 1861-1864.

(22) Gonze, X. First-principles responses of solids to atomic displacements and homogeneous electric fields: Implementation of a conjugate-gradient algorithm. *Phys. Rev. B* **1997**, *55*, 10337-10354.

(23) Kresse, G.; Furthmüller, J. Efficient iterative schemes for *ab initio* total-energy calculations using a plane-wave basis set. *Phys. Rev. B* **1996**, *54*, 11169-11186.

(24) Kresse, G.; Hafner, J. *Ab initio* molecular dynamics for liquid metals. *Phys. Rev. B* **1993**, *47*, 558-561.

(25) Kresse, G.; Furthmüller, J. Efficiency of *ab-initio* total energy calculations for metals and semiconductors using a plane-wave basis set. *Comput. Mater. Sci.* **1996**, *6*, 15-50.